Supporting Information

Preparation of solid solution and layered IrO_x-$Ni(OH)_2$ oxygen evolution catalysts: Towards optimising iridium efficiency for OER.

Jonathan Ruiz Esquius[a], Gerardo Algara-Siller[b], Ioannis Spanos[c], Simon J. Freakley[a,d], Robert Schlögl[b,c] and Graham J. Hutchings[*a]

[a] School of Chemistry, Cardiff Catalysis Institute, Cardiff University, Main Building, Park Place, Cardiff CF10 3AT, UK.

[b] Department of Inorganic Chemistry, Fritz-Haber-Institute der Max-Planck-Gesellschaft, Faradayweg 4-6, Berlin, 14195, Germany.

[c] Department of Heterogeneous Reactions, Max Planck Institute for Chemical Energy Conversion, Stiftstrasse 34-36, Mulheim an der Ruhr, 45470, Germany.

[d] Department of Chemistry, University of Bath, Claverton Down, Bath, BA2 2AY, UK.

* Hutch@cardiff.ac.uk

List of contents

1. Catalyst characterisation

IrNi-LY, IrNi-HD and IrO_x catalysts morphology characterisation by XRD and TEM

Transmission electron microscopy (TEM) characterisation confirmed the amorphous morphology of IrO_x and IrNi-HD catalysts (Figure S1a and S1b, respectively). TiO_2 contamination not detected by XRD was observed for IrNi-HD as seldom and small (2 nm) TiO_2 crystals (Figure S1c), for which its origin cannot be accounted. Although the origin of this contaminant cannot be elucidated, due to the high concentration of nickel at the surface prone to corrosion under OER reaction conditions, it can be suggested that trace TiO_2 contamination has little effect on the catalytic performance towards OER. Thus, low activity and stability observed for IrNi-HD was assigned to surface Ni. No TiO_2 contamination was detected for IrO_x or IrNi-LY. In accordance with XRD characterisation, a mixture of α/β-$Ni(OH)_2$ was observed for IrNi-LY (Figure 1).

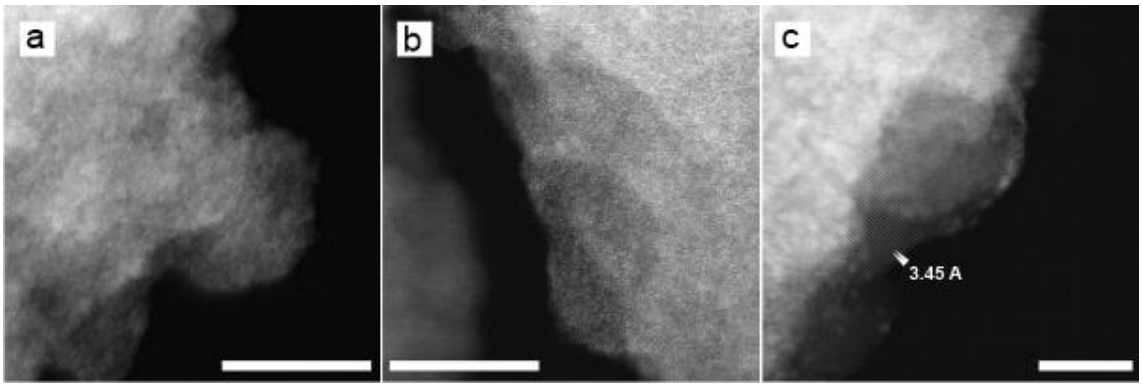

Figure S1. a) and b) High resolution scanning electron microscopy (STEM) image showing the homogenous amorphous nature of IrOx and IrNi-HD, respectively. c) two nanometer-sized TiO_2 crystals found in the material, although seldom. Scale bars corresponds to 10 nm.

The amorphous nature of IrO_x and IrNi-HD catalysts compared to IrNi-LY was also evidenced by the less defined rings and lower peak intensities obtained from electron diffraction patterns (Figure S2). Electron diffraction profiles obtained by TEM agrees with the XRD patterns in Figure S1. With IrO_x and IrNi-HD being of a generally amorphous nature, and IrNi-LY having a α/β-$Ni(OH)_2$ crystalline phase.

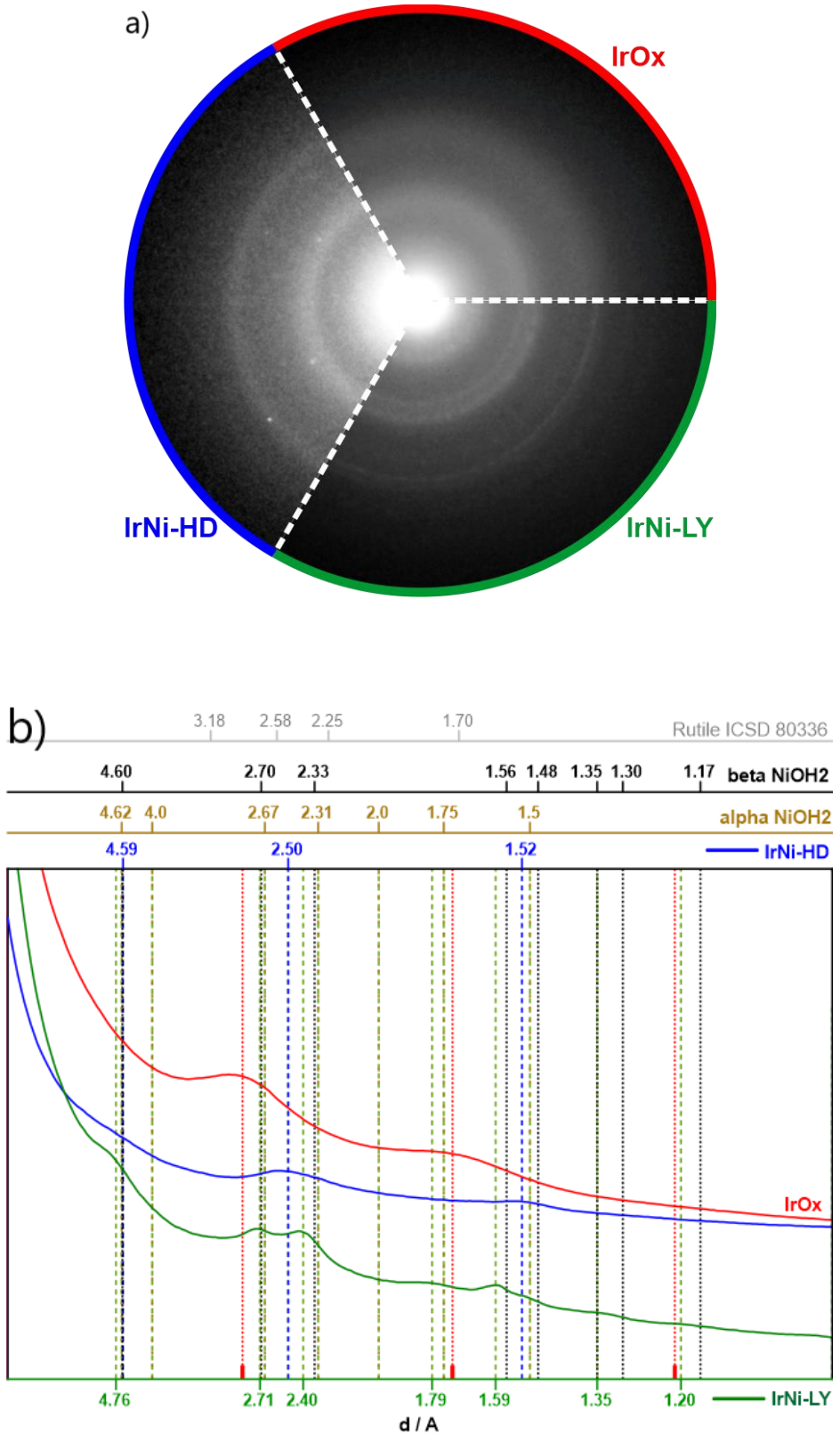

Figure S2. a) Electron diffraction patterns and b) represented as radial for IrNi-LY, IrNi-HD and IrO_x.

The presence of crystalline phases on synthesised IrNi-LY, IrNi-HD and IrO_x catalysts was assessed by XRD (Figure S3). XRD pattern for IrO_x shows a low-intense shoulder close to 34°, in agreement with XRD patterns reported for amorphous iridium oxo-hydroxides.[1] The XRD pattern recoded for IrNi-HD is similar to that of IrO_x, which in conjunction with TEM characterisation (Figure S1) confirmed IrNi-HD as amorphous. Extra XRD reflections associated to a mixture of α/β-$Ni(OH)_2$[2] were observe for IrNi-LY, in accordance with the synthetic procedure where a Ni-phase was first precipitated and used as support for IrO_x.

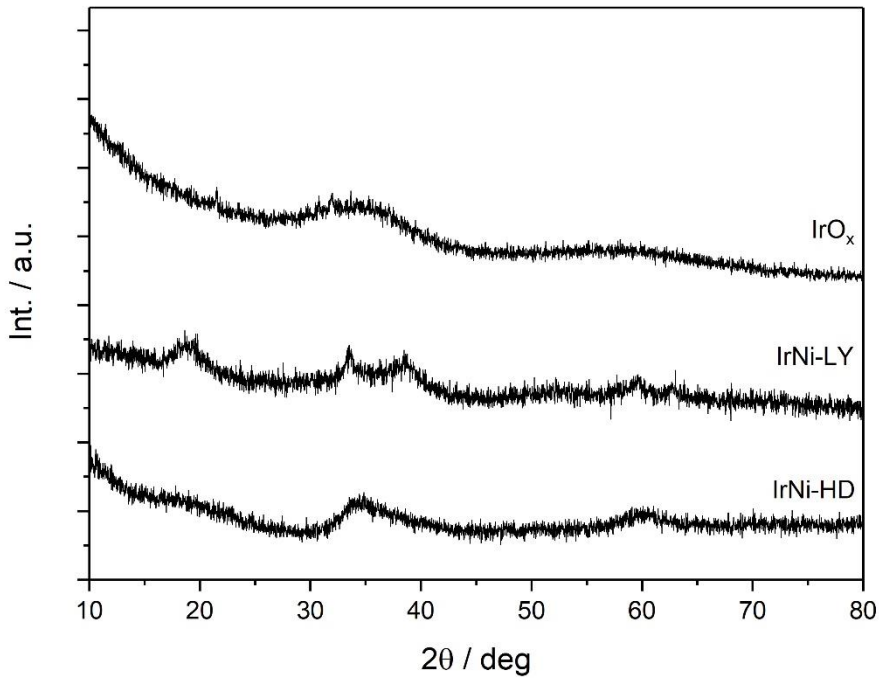

Figure S3. XRD pattern for prepared IrO_x, IrNi-LY and IrNi-HD catalysts after drying at room temperature.

Commercial rutile IrO_2 (Sigma Aldrich) characterisation

Commercial rutile IrO_2 from Sigma Aldrich was thoroughly characterised elsewhere.[3] It was confirmed the exclusive presence of Ir^{4+} and O^{2-} sites, in accordance with its stoichiometry. Performed characterisation was in good agreement with previous manuscripts: Only rutile IrO_2 phase (JCPDS-015-0876) was detected by XRD characterisation (Figure S4a), without the presence of metal Ir (JCPDS-006-0598) impurities;[4] Elemental XPS quantification using Ir(4f) and O(1s) peaks gave an Ir:O molar ratio of 0.49, in good agreement with the 0.5 for the stoichiometric oxide. Ir(4f) (Figure S1b) and O(1s) (Figure S4c) peaks were asymmetric, due to the conductive

properties of IrO_2, and centred at 61.9 eV and 530.0 eV respectively, both peaks could be fitted using Finite-Lorentzian and Gaussian-Lorentzian lineshapes described in literature before.[5]

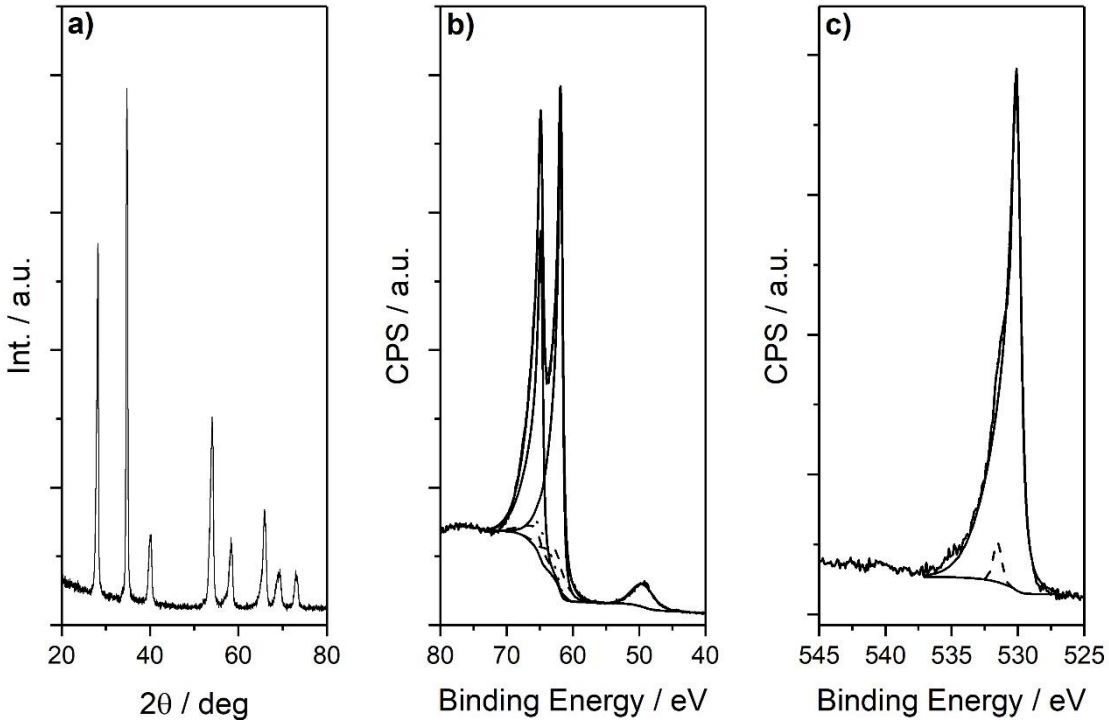

Figure S4. Characterisation performed on commercial rutile IrO_2 from Alfa Aesar. a) XRD pattern, b) Ir(4f) and c) O(1s) XPS peaks.

The catalytic activity towards OER of commercially supplied rutile IrO_2 was assessed in a flow cell in 0.1 M $HClO_4$.[6] The electrolyte was purged with Ar for 30 minutes before reaction. Linear sweep voltammetry (LSV, 1.20 V_{RHE} - 1.65 V_{RHE}, 5 $mV \cdot s^{-1}$, Figure S5a) and chronopotentiometry (CP, 10 $mA \cdot cm^{-2}$, Figure S5b) showed the poor activity and stability of rutile IrO_2. Additionally, cyclic voltammetry (CV, 0.7 V_{RHE} - 1.4 V_{RHE} at 50 $mV \cdot s^{-1}$, Figure S5c) showed no defined electronic transitions, in agreement with previous reports.[7]

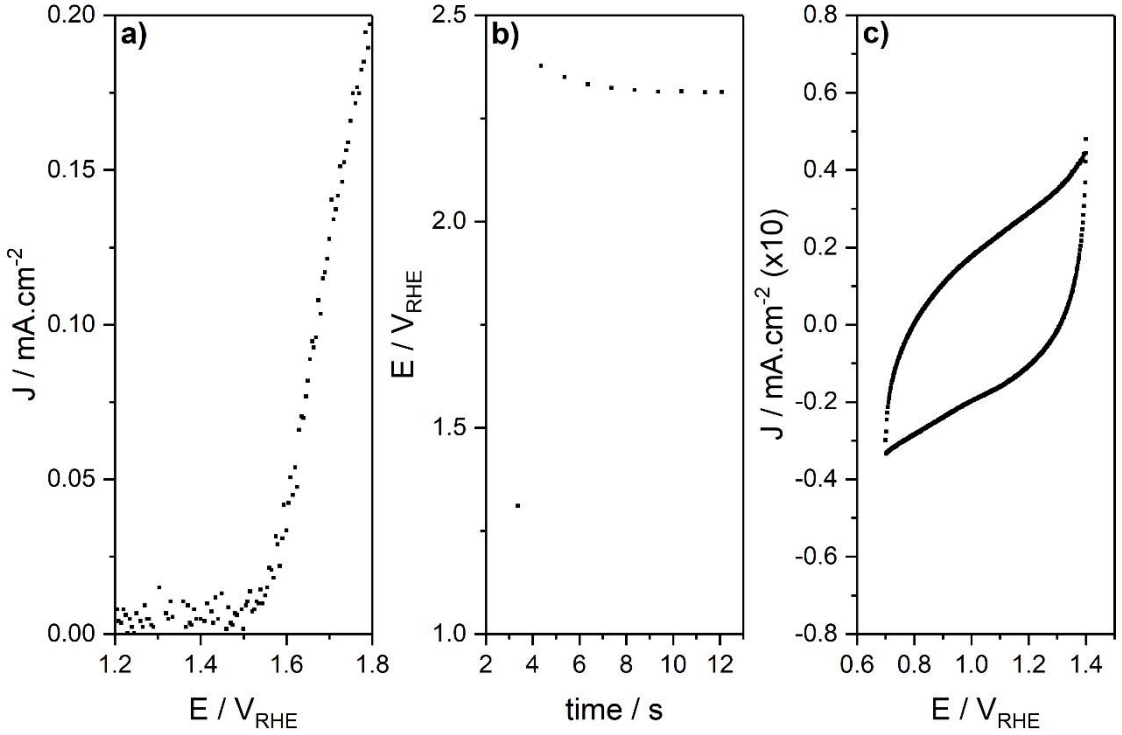

Figure S5. Catalytic performance of commercial rutile IrO_2 assessed by a) LSV (1.2 V_{RHE} - 1.8 V_{RHE}, 5 $mV \cdot s^{-1}$), b) CP (10 $mA \cdot cm^{-2}$) and c) CV (0.7 V_{RHE} - 1.4 V_{RHE} at 50 $mV \cdot s^{-1}$).

XAS analysis on catalysts supported on carbon cloth

Synthesised catalysts (IrO_x, IrNi-LY and IrNi-HD) and commercial rutile IrO_2 from Sigma Aldrich were drop-casted on carbon cloth (Sigracet 39 AA from fuel cell store)[8] following the same procedure used for the preparation of working electrodes for OER testing in a flow cell. 5 mg of catalyst were re-dispersed in 2.5 ml (1.23 ml water, 1.23 ml ethanol, 40 µl nafion solution). The mixture was sonicated for 30 min. 56 µl of catalyst ink were drop-casted on a 5 mm x 5 mm square of carbon cloth (Sigracet 39 AA, 50 $g \cdot m^{-2}$) to obtain a catalyst loading of 150 $mg_{cat} \cdot cm^{-2}$.

Samples supported on carbon cloth were placed in the sealed electrochemical cell,[9] and XAS spectroscopy in fluorescence at Ir L_3 edge measured without electrolyte. 5 scans were measured per sample, the average was used for data analysis. Athena and Artemis software packages[10] were used for XANES and EXAFS data analysis respectively. The first coordination shell (Ir-O bond distances) were calculated considering an IrO_6 octahedra with four equatorial and two axial oxygens[11] respectively (Table S1).

Table S1. EXAFS fitting parameters used for obtaining the first coordination shell. Iridium coordination was fixed to two axial and four equatorial Ir-O bonds. Amplitude reduction factor was obtained from fitting IrO_2 (amp = 0.78) and employed for $IrNiO_x$ synthesised samples.

Catalyst	Ir-$O_{(eq)}$ / Å	Ir-$O_{(ax)}$ / Å	Ir-$O_{(av)}$ / Å	σ^2 / Å^2	R / Å	E_0 / eV	R-factor
IrO_x	2.0236	1.9904	2.0126	0.0026 ± 0.0006	0.0085 ± 0.0081	10.9	0.002
IrNi-HD	2.0252	1.9920	2.0142	0.0021 ± 0.0007	0.0101 ± 0.0102	9.9	0.002
IrNi-LY	2.0290	1.9958	2.0179	0.0021 ± 0.0007	0.0139 ± 0.0099	10.5	0.002
Rutile IrO_2	1.9887	1.9555	1.9775	0.0015 ± 0.0013	-0.0264 ± 0.0187	11.3	0.006

2. Electrochemical Measurements

Cyclic Voltammetry

XPS and TEM catalyst characterisation indicates that the surface of IrNi-LY is essentially IrO_x. Cyclic voltammetry (CV) at high scan rates is especially sensitive to surface composition, with electronic transitions indicating electrochemically active species at the surface, and the curve area related to its concentration.[12, 13] Recorded CV (0.7 - 1.4 V_{RHE}, 50 $mV \cdot s^{-1}$) are presented in Figure S6. As reported for amorphous iridium oxo-hydroxides[12, 13] the Ir^{+3}/Ir^{+4} and Ir^{+4}/Ir^{+5} electronic transitions at 0.95 V_{RHE} and 1.25 V_{RHE} were observed for IrO_x. For IrNi-LY, the electronic transition are less pronounced and the curve area slightly decreases compared to IrO_x, indicating a lower concentration of electrochemically active sites, and indicative of the presence of surface nickel atoms as observed by the detected Ni corrosion during reaction (figure 6). The curve area significantly decreased, and no electronic transitions were observed for IrNi-HD, which can be correlated with the high concentration of nickel at the surface and the low concentration of active sites.

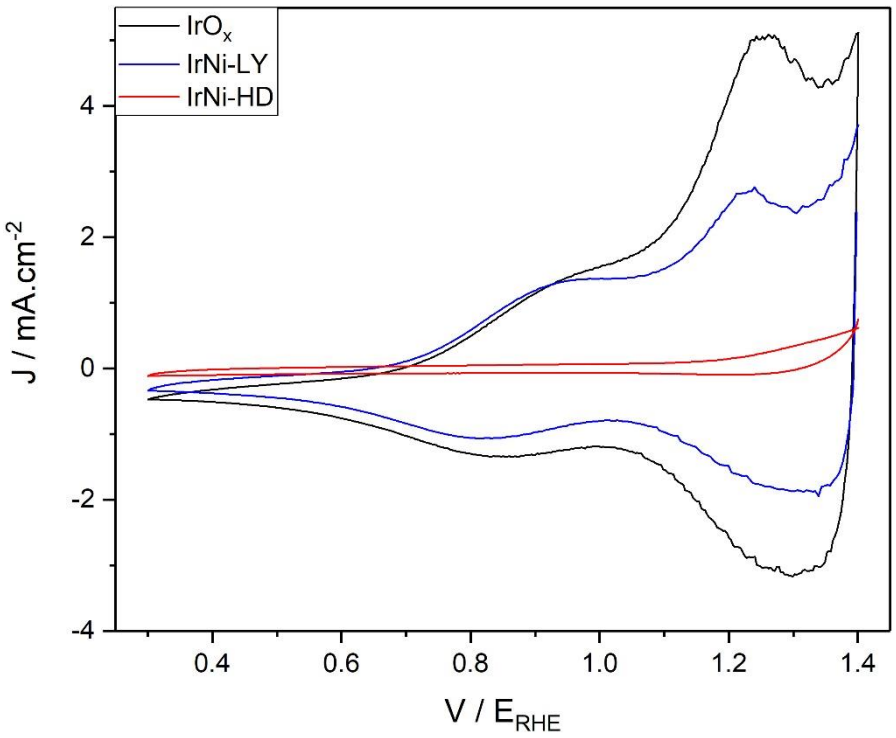

Figure S6. CV curves (0.3-1.4 V_{RHE}, 50 $mV \cdot s^{-1}$) recorded for synthesised IrO_x, IrNi-LY and IrNi-HD catalysts.

Tafel slope determination

Tafel slope, obtained from plotting the ohmic drop corrected overpotential against the logarithm of the current density under semi-steady-state conditions, contains information about the reaction mechanism. By comparison with computed Tafel slopes, it is possible to correlate experimental values with the rate determining step. Tafel slopes for IrO_x, IrNi-LY and IrNi-HD catalysts was obtained from LSV measurements (1.4 - 1.5 V_{RHE}, 0.5 $mV \cdot s^{-1}$) (Figure S7). At low overpotential (1.44 - 1.50 V_{RHE}), measured Tafel slopes for IrO_x (41 $mV \cdot dec^{-1}$) and IrNi-LY (37 $mV \cdot dec^{-1}$) were in agreement with previously reported values (~ 40 $mV \cdot dec^{-1}$),[14] whilst a slightly higher values was observed for IrNi-HD (53 $mV \cdot dec^{-1}$) in agreement with other IrNi mixed oxide catalysts reported previously (~ 60 $mV \cdot dec^{-1}$).[15]

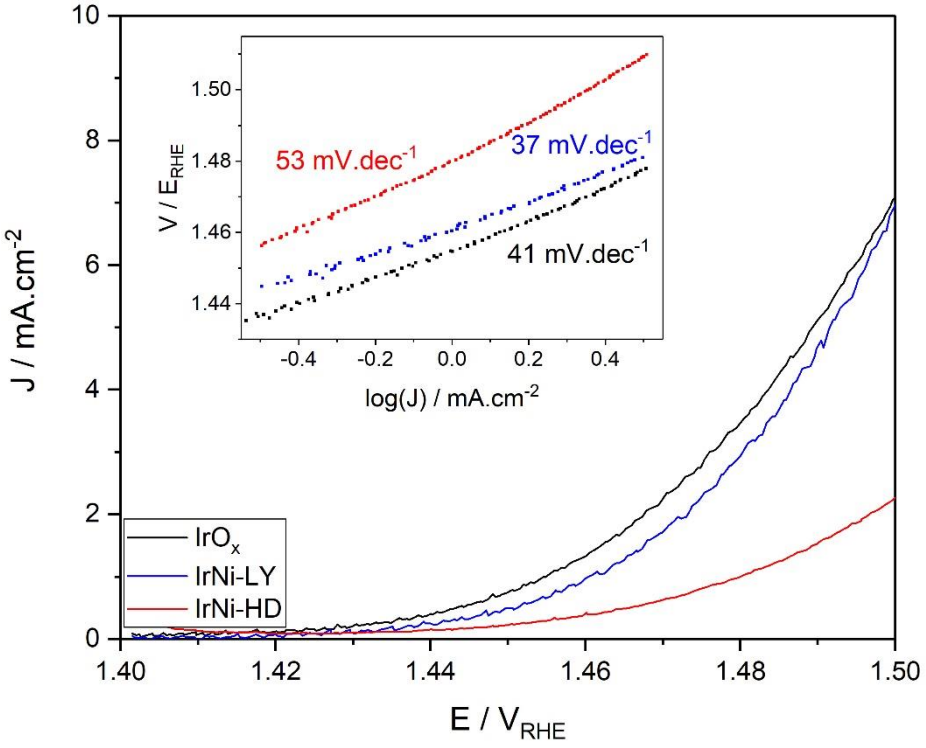

Figure S7. Semi-steady-state LSV polarization curves recorded between 1.4 and 1.5 V_{RHE} at 0.5 $mV \cdot s^{-1}$ for IrO_x, IrNi-LY and IrNi-HD catalysts and obtained Tafel slope at low overpotential (1.43 - 1.47 V_{RHE}).

Electrochemically active surface area

The electrochemically active surface area (ECSA) for IrNi-LY, IrNi-HD and IrO_x was measured by CV between 0.5 and 0.6 V_{RHE} to avoid the interference of Faradaic processes at different scan rates (2, 5, 10, 50 and 100 $mV \cdot s^{-1}$) (Figure S8a). The slope obtained from plotting the average between the anodic current density and the cathodic current density measured at the middle of the analysis window (0.55 V_{RHE}), $(J_{an} - J_{cat})/2$, against the scan rate is the double layer capacitance (C_{DL}) of the material (Figure S8b). The C_{DL} can be converted into ECSA by diving it by the specific capacitance in acidic condition ($C_{s,\,ac}$ = 0.035 $mF \cdot cm^{-2}$), ECSA = C_{DL} / $C_{s,\,ac}$. ECSA values of 0.006 cm^{-2}, 0.003 cm^{-2} and 0.001 cm^{-2} were obtained for IrNi-LY, IrNi-HD and IrO_x, respectively.

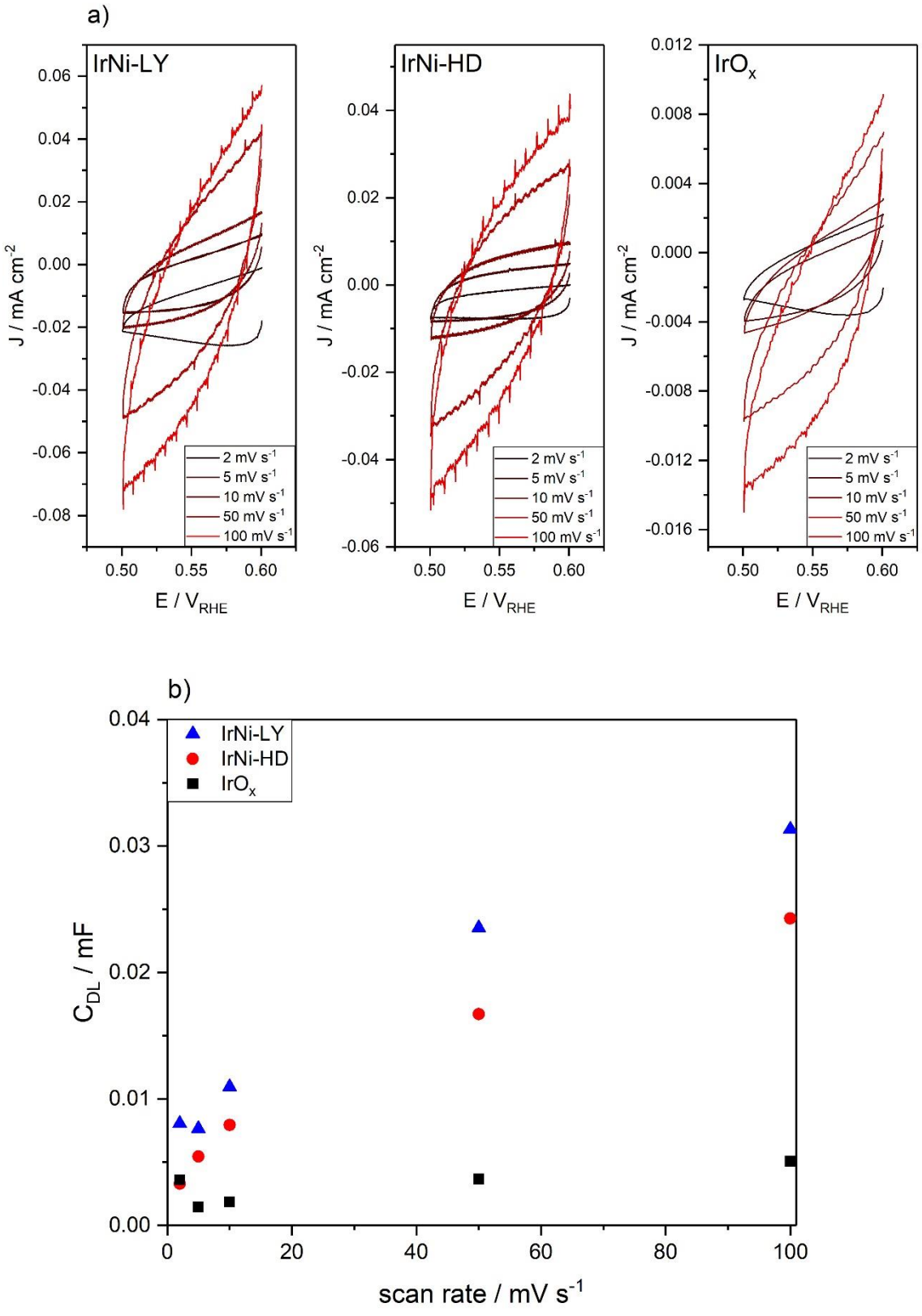

Figure S8. a) Double-layer capacitance measurements for the determination of ECSA and b) average between anodic and cathodic current density, (J_{an}-J_{cat})/2, plotted against CV scan rate.

Electrocatalytic activity towards OER

Synthesised IrO_x, IrNi-HD and IrNi-LY catalysts were assessed for OER. Intrinsic catalytic activity was determined in a conventional three electrode set up. The resemblance in the surface composition between IrO_x and IrNi-LY resulted in comparable catalytic activity and stability (Figure 5). Whilst, the activity and stability of IrNi-HD catalyst was compromised compared to IrO_x because of the high presence of nickel sites at the surface. When catalytic activity is normalised against the iridium mass, IrNi-LY presents higher activity than IrO_x (Figure S9). Moreover, comparing LSV measurements before and after CP (10 $mA \cdot cm^{-2}$, 2 h) confirmed the high catalytic stability of IrO_x and IrNi-LY catalysts against corrosion compared to IrNi-HD (Figure S9).

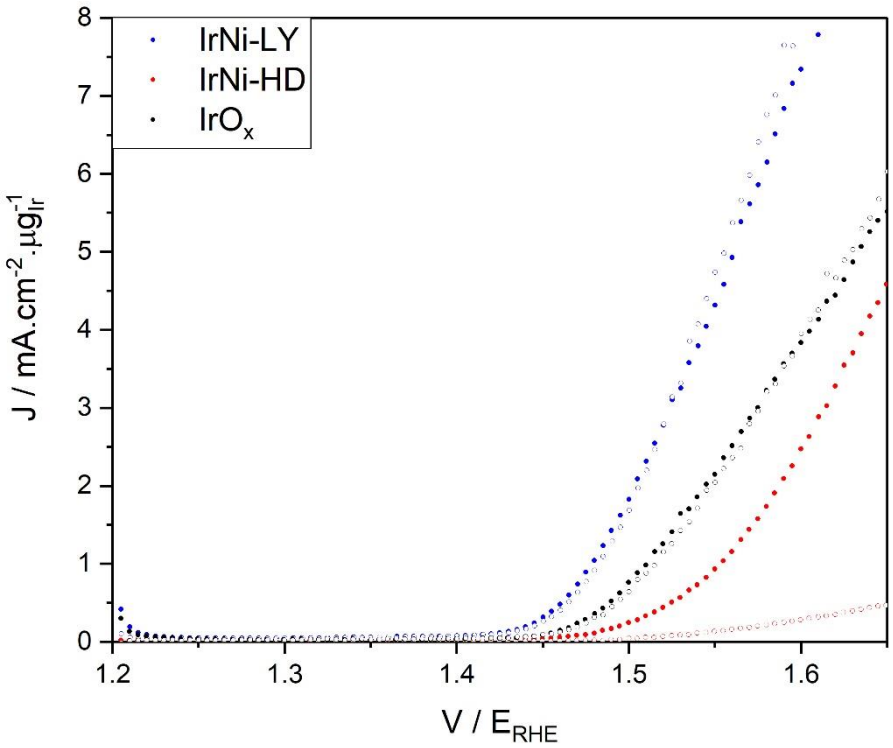

Figure S9. Iridium mass normalised catalytic activity towards OER for IrO_x, IrNi-LY and IrNi-HD determined by LSV (1.2 - 1.65 V_{RHE}) on a conventional three electrode setup before (solid circles) and after (empty circles) stability test (CP at 10 $mA \cdot cm^{-2}$, 2 h).

To relate the observed catalyst deactivation during CP (2 h, 10 $mA \cdot cm^{-2}$) to the iridium and nickel dissolution, OER was performed in a three electrode flow cell described previously in literature.[16] Metal dissolution (Ir and Ni) data is included in main text (figure 6). Intrinsic catalytic activity measured by LSV in the flow cell (Figure S10a) followed the same trend observed in the conventional cell, although the cell design was different, and

the working electrode tip was made of gold instead of glassy carbon. IrO_x and IrNi-LY presented comparable activity, whilst a significant decrease in activity was observed for IrNi-HD catalyst, which can be associated with the high concentration of nickel at the surface as confirmed by XPS characterisation, and the high nickel dissolution detected by *in situ* ICP during CP.

Catalytic activity towards OER vary with the catalyst mass, and hence it is not recommendable to only compare catalyst activity with catalytic activities normalised to the geometric surface area. Fabbri *et. al*.[17] discussed the catalytic activity of IrO_2 catalyst against the geometric surface area, the electrocatalytic active surface area (ECSA) and the iridium mass, it was concluded that the best catalytic activity comparison is achieved by normalising against the iridium mass. To obtain the iridium mass on the electrode, thermogravimetric analysis (TGA) were performed on synthesised samples (30 - 800 °C, 5 $C \cdot min^{-1}$, N_2) (Figure S10b). It was assumed that the mass loss corresponded to the loss of chemy- and physiosorbed water, yielding IrO_2 and NiO. Iridium mass normalised activities for synthesised catalyst (Figure S10c) show the higher activity of IrNi-LY when compared to IrO_x.

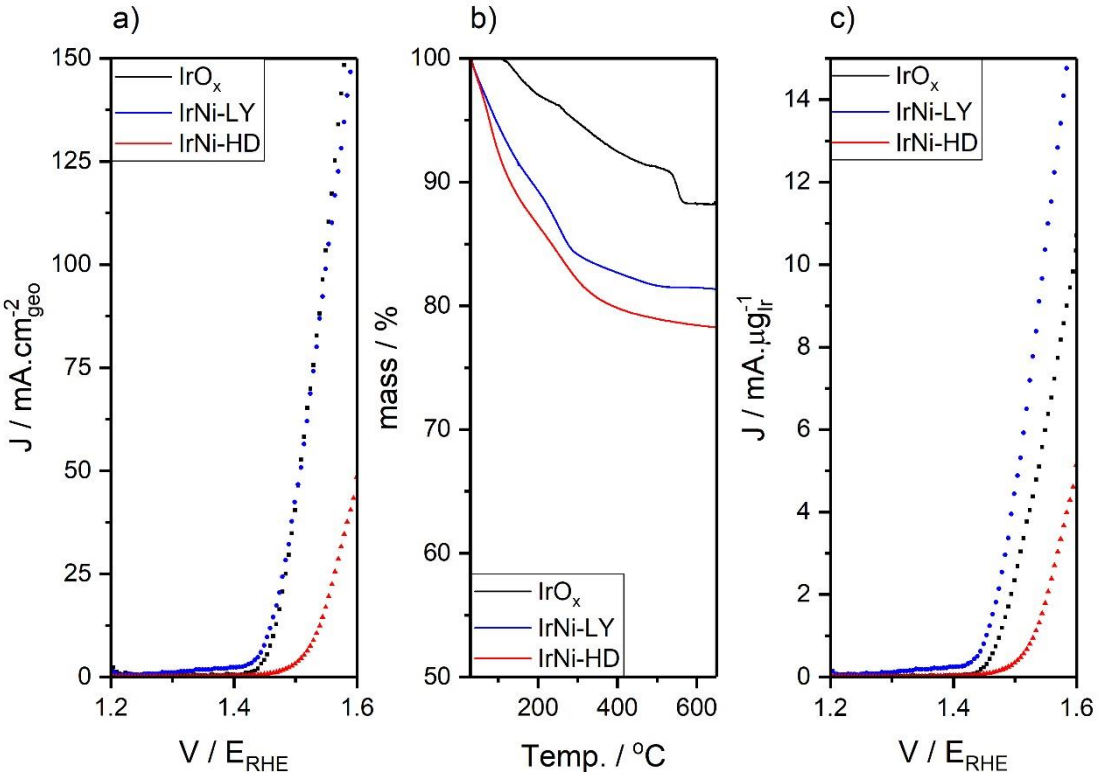

Figure S10. a) Intrinsic catalytic activity obtained from LSV measurements for synthesised catalysts performed in a 3-electrode flow cell connected to an ICP, b) TGA for synthesised samples and c) Iridium mass normalised LSV activities.

Iridium and Nickel dissolution during OER

Iridium and nickel dissolution during chronopotentiometry (CP, 10 $mA \cdot cm^{-2}$, 2 h) was monitored in a three electrode flow cell connected to an ICP. The ICP was calibrated prior to reaction for Ir and Ni using standardised solutions, background was measured by flowing electrolyte (0.1 M $HClO_4$, 1.2 $ml \cdot min^{-1}$) through the cell for 5 minutes at open circuit potential (OCP). Determined metal dissolution for IrO_x, IrNi-LY and IrNi-HD can be found in Table S2. IrO_x and IrNi-LY showed similar iridium dissolution, while a fourfold increase in iridium dissolution was detected for IrNi-HD. Ni corrosion was considerably higher for IrNi-HD compared to IrNi-LY. This in accordance with catalyst characterisation and further suggesting that the surface of IrNi-LY is composed mainly of IrO_x while an equimolar amount of Ir and Ni is present at the surface of IrNi-HD.

Table S2. *Online* iridium and nickel dissolution during CP (10 $mA \cdot cm^{-2}$, 2 h) measured in a 3-electrode flow cell set up attached to an ICP.

Catalyst	Iridium dissolution / ng	Nickel dissolution / ng
IrO_x	95	0
IrNi-LY	100	800
IrNi-HD	380	2000

References

1. J. Ruiz Esquius, D. J. Morgan, I. Spanos, D. G. Hewes, S. J. Freakley, G. J. Hutchings, Effect of base on the facile hydrothermal preparation of highly active IrO_x oxygen evolution catalysts, *ACS Applied Energy Materials*, **2020**, 3, 800-809.
2. D. S. Hall, D. J. Lockwood, C. Bock, B. R. MacDougall, Nickel hydroxides and related materials: a review of their structures, synthesis and properties, *Proceedings Royal Society A*, **2014**, 471, 792.
3. V. Pfeifer, T. E. Jones, J. J. Velasco Vélez, C. Massué, R. Arrigo, D. Teschner, F. Girgsdies, M. Scherzer, M. T. Greiner, J. Allan, M. Hashagen, G. Weinberg, S. Piccinin, M. Hävecker, A. Knop-Gericke, R. Schlögla, The electronic structure of iridium and its oxides, *Surface and Interface Analysis*, **2016**, *48* (5), 261-273.
4. V. Pfeifer, T. E. Jones, J. J. Velasco Velez, C. Massué, M. T. Greiner, R. Arrigo, D. Teschner, F. Girgsdies, M. Scherzer, J. Allan, M. Hashagen, G. Weinberg, S. Piccinin, M. Hävecker, A. Knop-Gericke, R. Schlögl, The electronic structure of iridium oxide electrodes active in water splitting, *Physical Chemistry Chemical Physics*, **2016**, *18* (4), 2292-2296.
5. S. J. Freakley, J. R. Esquius, D. J. Morgan, The X-ray photoelectron spectra of Ir, IrO_2 and $IrCl_3$ revisited, *Surface and Interface Analysis*, **2017**, *49* (8), 794-799.
6. I. Spanos, A. A. Auer, S. Neugebauer, X. Deng, H. Tüysüz, R. Schlöegl, Standardized Benchmarking of Water Splitting Catalysts in a Combined Electrochemical Flow Cell/Inductively Coupled Plasma-Optical Emission Spectrometry (ICP-OES) Setup, *ACS Catalysis*, **2017**, 7, 3768-3778.
7. Y. lee, J. Suntivich, K. J. May, E. E. Perry, Y. Shao-Horn, Synthesis and activities of rutile IrO_2 and RuO_2 nanoparticles for oxygen evolution in acid and alkaline solutions, *The Journal of Physical Chemistry Letters*, **2012**, 3 (3), 399-404.
8. Fuel Cell Store, www.fuelcellstore.com
9. C. Genovese, M. E. Schuster, E. K. Gibson, D. Gianolio, V. Posligua, R. Grau-Crespo, G. Cibin, P. P. Wells, D. Garai, V. Solokha, S. Krick Calderon, J. J. Velasco-Velez, C. Ampelli, S. Perathoner, G. Held, G. Centi, R. Arrigo, Operando spectroscopy study of the carbon dioxide electro-reduction by iron species on nitrogen-doped carbon, *Nature Communications*, **2018**, 9 (935), 1-12.
10. Demeter: XAS Data Processing and Analysis, www.bruceravel.github.io/demeter.
11. A. M. Cruz, LI. Abad, N. M. Carretero, J. Moral-Vico, J. Fraxedas, P. Lozano, G. Subias, V. Padial, M. Carballo, J. E. Collazos-Castro, N. Casañ-Pastor, Iridium Oxohydroxide, a Significant Member in the Family of Iridium Oxides. Stoichiometry,

Characterization, and Implications in Bioelectrodes, *The Journal of Physical Chemistry C*, **2012**, 116 (8), 5155-5168.

12. L. Ouattara, S. Fierro, O. Frey, M. Koudelka, C. Comninellis, Electrochemical comparison of IrO_2 prepared by anodic oxidation of of pure iridium and IrO_2 prepared by thermal decomposition of H_2IrCl_6 precursor solution, *Journal of Applied Electrochemistry*, **2009**, 39 (8), 1361-1367.
13. J. Juodkazyte, B. Sebeka, I. Valsiunas, K. Juodkazis, Iridium anodic oxidation to Ir(III) and Ir(IV) hydrous oxides, *Electroanalysis*, **2005**, 17 (11), 947-952.
14. T. Shinagawa, A. T. Garcia-Esparza, K. Takanabe, Insight on Tafel slopes from a microkinetic analysis of aqueous electrocatalysis for energy conversion, Scientific Reports, 2015, 5 (13801), 1-21.
15. S. Xu, Y. Liu, J. Tong, W. Hu, Q. Xia, Iridium-Nickel composite oxide catalysts for oxygen evolution reaction in acidic water electrolysis, *Russian Journal of Electrochemistry*, **2016**, 52 (11), 1021-1031.
16. I. Spanos, A. A. Auer, S. Neugebauer, X. Deng, H. Tüysüz, R. Schlögl, Standarized benchmarking of water splitting catalysts in a combined electrochemical flow cell/ICP-OES setup, *ACS Catalysis*, **2017**, 7, 3768-3778.
17. E. Fabbri, A. Habereder, K. Waltar, R. Kötz, T. J. Schmidt, Developments and perspectives of oxide-based catalysts for the oxygen evolution reaction, *Catalysis Science & Technology*, **2014**, 4, 3800-3821.